Morphodynamic Profiling of Protrusion Phenotypes

M. Machacek and G. Danuser

Laboratory for Computational Cell Biology, Department of Cell Biology, The Scripps Research Institute, La Jolla, CA 92037

ABSTRACT   We propose a framework for tracking arbitrary complex cell boundary movements, relying on a unique definition of protrusion and retraction as the pathlength a virtual edge marker traverses when moving continuously perpendicular to the cell boundary. We introduce the level set method as a numerical scheme to reconstruct continuous boundary movement in time-lapse image sequences with finite time sampling. For moderately complex movements, we describe a numerically less expensive method that satisfactorily approximates the definition. Densely sampled protrusion and retraction rates were accumulated in space-time charts revealing distinct morphodynamic states. Applying this technique to the profiling of epithelial cell protrusion we identified three different states. In the *I-state*, long cell edge sectors are synchronized in cycles of protrusion and retraction. In the *V-state* random bursts of protrusion initiate protrusion waves propagating transversally in both directions. Cells switch between both states dependent on the Rac1 activation level. Furthermore, the persistence of transversal waves in the *V-state* depends on Arp2/3 concentration. Inhibition of PAK shifts cells into a *λ-state* where continuous protrusion is occasionally interrupted by self-propagating ruffles. Our data support a model where activation of Rac1 mediates the propagation of protrusion waves, whose persistence depends on the relative abundance of activated Arp2/3 and polymerizable G-actin.

INTRODUCTION

Cell morphology is the complex output of interconnected mechanical and regulatory networks. The driving machinery of cell morphology, the cytoskeleton, is critical for a variety of cell functions such as cell migration, proliferation, and apoptosis. Therefore, cell morphology is widely used as the readout of cell states in investigations of molecular pathways that affect cell functions via the cytoskeleton. Surprisingly, however, rigorous methodology to analyze the morphology of cells is lacking. Most studies that identify molecular functions based on morphological phenotypes rely on relatively simple and ad hoc approaches, where cell morphology is evaluated according to the judgment of the observer. The lack of more objective measures may be explained with the challenges to define unique morphological signatures that pinpoint functionally relevant differences between a vast variety of cell shapes and dynamics.

One of the obvious functions where readouts of morphological behavior have been exploited is migration. Using a computer-assisted segmentation of the complete three-dimensional cell surface, Wessels and Soll developed a tool to distinguish the effects of mutations of different molecular pathways involved in the migration of *Dictyostelium discoideum* (1,2). The crucial point in these studies was to extract morphological descriptors with optimal discrimination power from the three-dimensionally reconstructed cell. Although a large number of elaborate shape descriptors were used, no attempt was made to characterize cell migration as a dynamic process and to define descriptors

that capture different modes of cell shape evolution over time. Intuitively, the shape evolution should be the most informative indicator of different molecular mechanisms related to cell migration.

Such morphodynamic measures have been used on a more local level to dissect pathways involved in cell protrusion activity. In many cases it is quite easy to extract the cell contour from images, allowing contour-based analysis of morphological dynamics. For example, Waterman-Storer et al. (3) used the ratio of protrusive to quiescent cell perimeter as a measure of protrusion activity. Alternatively, once the cell contour is identified, rates of protrusion can also be estimated based on the binary difference image of the cell area between consecutive time points. This approach was applied in recent studies of cell spreading dynamics (4), actin transport to protruding lamellipodia (5), the formation of filopodia downstream of SCAR (6), and the role of cofilin as a promoter of actin polymerization leading to protrusion (7). Although the cell area difference allows a consistent estimation of morphological changes, it cannot differentiate between fundamentally different modes of protrusion (Fig. 1, *A–C*).

Alternatively, protrusion rates can be measured at multiple locations of the cell boundary. Rottner et al. (8) studied the role of VASP activation in protrusion dynamics by placing segments (typically 2–5-μm wide) normal to the boundary and measuring the displacement of the boundary inside the segments. An intensity measurement of GFP-VASP in the same segment provided information on the coupling between protein activity and protrusion. Using the same approach, Rotsch et al. (9) related protrusion dynamics to the local elasticity of the adjacent cytoskeleton. Instead of direct displacement tracking, the cell boundary can be analyzed
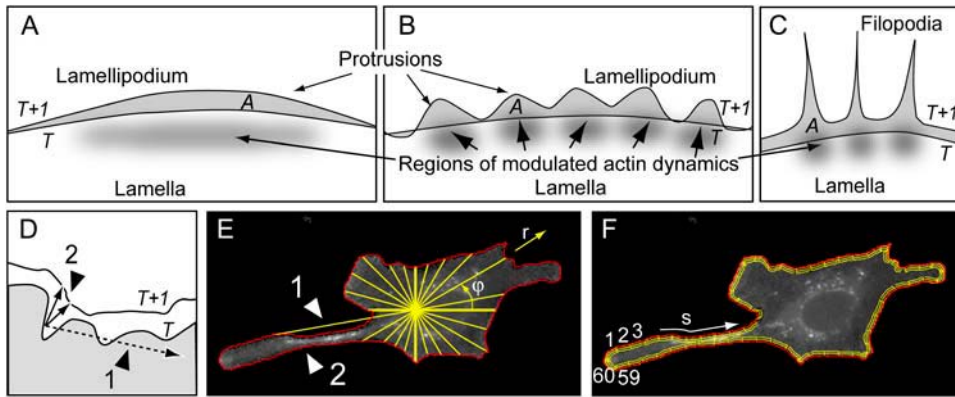
FIGURE 1 Problems of quantifying cell morphological changes (*A*–*C*). A frequently used measure of morphological changes is the cell area difference A between two time points. This parameter cannot capture local variations in the cell shape and thus is incapable of distinguishing many obvious morphodynamic phenotypes. (*D*) Morphological changes quantified by pointwise measurement of boundary displacements. The main difficulty of this method is defining the direction of displacement. In areas of strong boundary deformation, the normal direction is not meaningful (*arrowhead 1*) and any other choice is arbitrary (*arrowhead 2*). (*E*) Morphological changes in polar coordinates are measured by length variations of the radial coordinate r. For noncircular cell outlines this measurement is not unique (*arrowhead 1*) and the spatial resolution of the measurement varies substantially (*arrowhead 2*). (*F*) We propose a coordinate system based on the run length s of the boundary to avoid the polar coordinate-associated problems. Image courtesy of P. Nalbant.

with kymographs. Totsukawa et al. (10) used this method to identify the differential roles of MLCK and ROCK in regulating membrane protrusion, and Bear et al. (11) used it to investigate the role of Ena/VASP proteins in fibroblast protrusion and motility regulation. Hinz et al. (12) applied kymograph analysis to derive lamellipodia protrusion velocity and switching frequency between protrusion and retraction to quantify cell dynamics. The major shortcoming in all these approaches is that the local direction of the boundary displacement or the kymograph orientation has to be set manually. Apart from being tedious, this can be ambiguous in regions with strong boundary deformation (Fig. 1 *D*). The problem is alleviated for special cases such as for cell spreading assays where cells tend to have a circular outline. Under these conditions, protrusion can be estimated as the radial boundary displacement in a polar coordinate system with the origin in the cell center (13). Automation of the displacement measurement becomes straightforward, allowing protrusion analysis with high temporal and spatial resolution. However, this approach does not work for cells with more complex shapes and morphological dynamics (Fig. 1 *E*).

An obvious way to estimate morphological changes would be to track the displacement of individual markers on the cell boundary. Apart from the difficulty of identifying such membrane markers, the membrane itself is a very dynamic structure, so that tracks of individual membrane domains, like clusters of fluorescently labeled receptors, do not necessarily report cell morphological changes.

In view of the limitations of these existing approaches we decided to establish novel measures of protrusion and retraction activity to investigate the spatial and temporal coordination of cell boundary dynamics and to link it to specific molecular pathways via intervention studies. The goal was to track these morphological changes of the cell boundary in an automated fashion and with high resolution. In the following section we propose two methods to track

cell boundary displacements of arbitrary complexity with theoretically unlimited resolution. By accumulating dense displacement measurements along the cell edge over many frames in space-time maps, we were able to identify clearly distinguishable morphodynamic phenotypes despite the seemingly chaotic protrusion activity of many migrating cells. We exploited this possibility to classify the dynamics of leading edge movement in polarized epithelial cells, where we discovered oscillatory patterns of protrusion and retraction. Oscillations were in synchrony over long sectors of the cell edge or propagated transversally, dependent on the level of active Rac1. We also found the patterns varying with different levels of Arp2/3 and PAK activity, supporting a model that relates the morphodynamics of protruding edges to regulatory elements of actin polymerization in a network dominated by dendritic nucleation (14).

METHODS

Definition of protrusion and retraction

Our tracking method distinguishes between the tangential and normal components of boundary displacement. The tangential component does not contribute to the movement of the cell boundary. Therefore, we define cell protrusion and retraction as the boundary velocity in the direction normal to the cell boundary (Def. 1).

Given a sequence of cell boundaries extracted from a time-lapse series of cell images, protrusion and retraction rates are thus obtained by measuring the local boundary displacement according to Def. 1 and multiplying it with the frame rate. If the frame rate is sufficiently high the measurement is straightforward and a unique solution can be found. In practice, however, the time resolution is generally not sufficient to apply Def. 1 directly (Fig. 2 *A*). In the following sections we present two methods for displacement measurements between two arbitrary shaped curves. The central idea of the first method is to reconstruct the evolution of the cell boundary between two consecutive frames so that Def. 1 can be applied in a continuous fashion thereby avoiding the generation of topological conflicts (Fig. 2 *B*). In the second method we propose to slightly relax Def. 1 to obtain a simpler algorithm without the need to reconstruct the boundary evolution.
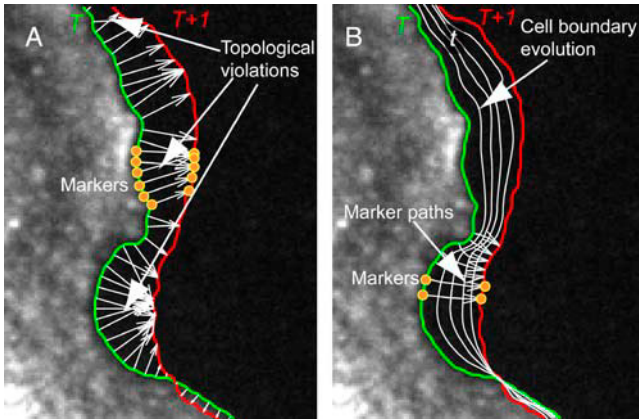
FIGURE 2   Definition of terms used for the morphodynamic measurements proposed in this article. (*Markers*) Virtual particles placed on the boundary at time point *T*. (*Marker path*) Trajectory of a marker between *T* and *T* + 1. Multiplying marker pathlength (displacement) with the frame rate yields the protrusion and retraction velocities. The difficulty of morphodynamic measurements is finding a rule to obtain consistent marker paths for all boundary shapes. (*A*) Following the normal direction, marker paths can cross (topological violation). (*B*) Topological violation is avoided by using continuous normal propagation of the cell boundary to find consistent marker paths between *T* and *T* + 1.

Protrusion and retraction estimation by boundary evolution between two time points: level set method

The level set method (LSM) is a well-established method for the description of complex boundaries and their evolution. It was originally introduced by Osher and Sethian (15) and has since been applied to a wide range of problems in fluid dynamics, combustion, image processing, material sciences, control theory, and others. The LSM has two crucial properties that allow performing cell morphodynamic measurements according to Def. 1: i), it can efficiently handle complex boundaries, and ii), it continuously propagates them in their normal direction.

Given the cell boundaries (Γ_T, Γ_{T+1}) in two consecutive frames at *T* and *T* + 1, the LSM provides the means to propagate the boundary Γ_T until it aligns with Γ_{T+1}. This yields intermediate cell boundaries on which we can define a set of evolving markers whose integrated paths represent a measure for the local boundary displacement (Fig. 2 *B*). Our starting point is the two-dimensional cell boundary $\Gamma_T(x, y) \in \mathbb{R}^2$. Following the LSM, Γ_T is embedded into a three-dimensional surface $\phi_T(x, y) \in \mathbb{R}^3$, called the level set, which is defined as the distance function to Γ_T, i.e., the value of ϕ_T at a location (x, y) is given by the distance to the closest point of the boundary $\Gamma_T(x, y)$ (Fig. 3). Locations inside the cell have positive distance values; locations outside have negative values. The level set at *T* + 1 is constructed in the same fashion. Once ϕ_T and ϕ_{T+1} are calculated ϕ_T is propagated into ϕ_{T+1} by the evolution equation

$$\frac{\partial \phi_t(x, y, t)}{\partial t} + F(\phi_t, t)|\nabla \phi_t(x, y, t)| = 0,$$
$$\phi_t(x, y, t = T) = \phi_T(x, y), \tag{1}$$

where *F* is the speed of the level set. From Eq. 1 we obtain the level set evolution ϕ_t, $t \in [T, T+1]$, from which the cell boundary Γ_t at any intermediate time point *t* can be retrieved as the zero level of the level set
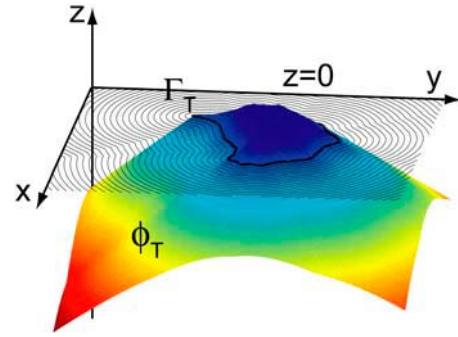
$$\Gamma(t) = \{(x, y)|\phi_t(x, y, t) = 0\}. \tag{2}$$

FIGURE 3   The principal idea of the level set method. The cell boundary Γ_T is embedded in the level set function ϕ_T, defined as the distance function of the boundary. To visualize the level set function ϕ_T, the distance from the cell outline is plotted on the *z* axis. The entire level set is propagated along its gradient $\nabla \phi_t$, $T \leq t \leq T+1$ according to Eq. 1 and evolved into the level set ϕ_{T+1} embedding the cell boundary Γ_{T+1}. See Movie 1 in the Supplementary Material for an animated evolution sequence of the level set function ϕ_t and its corresponding zero level curve Γ_t.

Notice that Eq. 1 constricts surface changes to the direction of the surface gradient. This applies, of course, also to the evolution of the zero level, so that the propagation of Γ_T into Γ_{T+1} intrinsically follows our definition of protrusive and retractive deformation of the plasma membrane evolving continuously in the direction perpendicular to the cell boundary. Movie 1 in Supplementary Material exemplifies the concept of boundary evolution by the LSM for the test case of an ellipse mapped on a second ellipse rotated by 90°.

The crucial step in LSM is to choose an adequate speed function *F* so that the cell boundary Γ_t evolves with desired characteristics and converges to the boundary Γ_{T+1} at the next frame, i.e.:

$$\lim_{\phi_t \to \phi_{T+1}} F = 0 \, \forall \, (x, y). \tag{3}$$

The simplest speed function that satisfies Eq. 3 moves the cell boundary at a speed proportional to its distance from the boundary at the next time point:

$$F_d = \phi_t - \phi_{T+1}. \tag{4}$$

After obtaining the boundary evolution, a set of *N* markers (x_i^T, y_i^T), $i = 1..N$ is defined on Γ_T, and their paths from Γ_T to Γ_{T+1} are calculated by integrating the orthogonally propagated steps $(x_i^t, y_i^t) \to (x_i^{t+1}, y_i^{t+1})$, $t = T..T+1$, $i = 1..N$ (Def. 1). Fig. 4 gives a summary of the steps involved in computing the boundary displacement based on the boundary evolution as estimated by the LSM.

Numerical procedure

Numerical schemes to solve Eq. 1 are well established (16–18). We used a finite difference scheme because of the moderate implementation complexity and relatively high computational efficiency. The term in Eq. 1 containing the spatial derivatives was approximated by a second-order scheme as described in Osher and Sethian (15). Time integration was achieved with a forth-order Runge-Kutta scheme with adaptable time step. The grid size has to be chosen such that the cell outline is resolved with sufficient detail. A resolution increase beyond this point will not improve the accuracy of boundary evolution but only prolong the computation unnecessarily. We found that all cell shapes studied in this article could be satisfactorily accommodated with a computational grid size of 3 × 3 pixels. For termination of the level set evolution we computed the Frobenius norm *r* of the difference *D* between the target function ϕ_{T+1} and the propagated level set function ϕ_t,
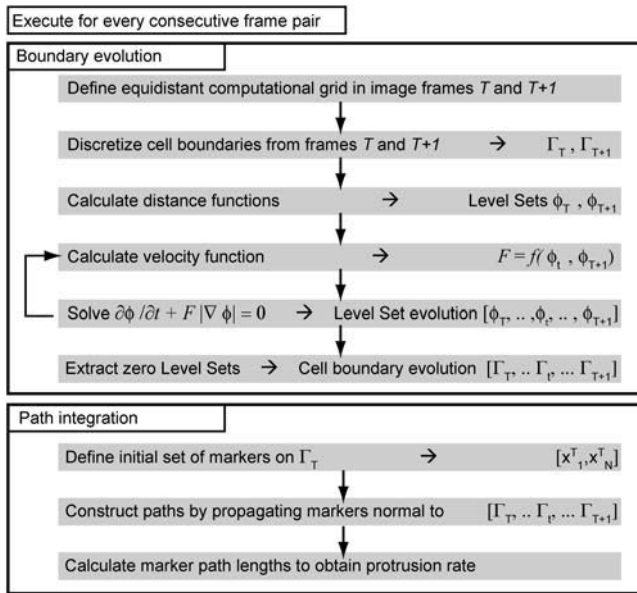
FIGURE 4   Level set algorithm.

$$r = \left(Tr(D^{\mathrm{T}}D)\right)^{1/2}, \quad D = \phi_{\mathrm{T+1}} - \phi_{\mathrm{t}}, \qquad (5)$$

where $Tr()$ denotes the trace of a matrix and is defined as the sum of the matrix diagonal elements. Note that the square of the Frobenius norm r is equivalent to the square sum of all elements of the difference matrix D. Therefore, the average difference between the evolving level set and the target function at each node of the computational grid can be estimated by r/N_{g}, where N_{g} is the number of grid nodes. The norm was compared to a fixed threshold, below which the evolution procedure was halted. The value of the threshold was determined empirically to balance computational time versus accuracy and was set to $r = 5$ pixels for all experiments.

Protrusion estimation by approximate solution: mechanical model

We wished to find a simpler and faster-to-implement method that still generated topologically correct and practically satisfactory results as an alternative to the LSM. As shown in Fig. 2, the problem of using the normal direction to estimate boundary displacements is that marker paths can cross. Specifically, in boundary sections with strong deformations the normal direction is inappropriate to approximate the true displacement direction. The intersection of the normal direction with the boundary in the next time point will either not exist (Fig. 1 *D*, *arrow 1*) or locate far from the nearest boundary position in the next time point, which, in this particular geometrical configuration, represents the most likely corresponding marker position. In view of these issues, we formulated our second approach as to measure boundary displacements in the normal direction, and thus to satisfy Def. 1, only as long as the topology of the marker paths was preserved. If the result caused a permutation in the marker sequence we relaxed Def. 1 allowing the marker path to deviate from the normal direction, thus maintaining the correct marker sequence. To accomplish this, we constructed a mechanical system with markers connected by two kinds of springs: torsion springs that enforce the normal direction and linear springs that avoid the crossover of neighboring marker paths (Fig. 5).

Given the cell boundaries at two consecutive time points T and $T + 1$, we defined a set of N spatially fixed markers $\underline{x}_i^{\mathrm{T}} = (x_i^{\mathrm{T}}, y_i^{\mathrm{T}})$, $i = 1..N$ on the boundary at T and a corresponding set of N markers $\underline{x}_i^{\mathrm{T+1}}$, $i = 1..N$ with unknown positions on the boundary at $T + 1$. Together, these indices
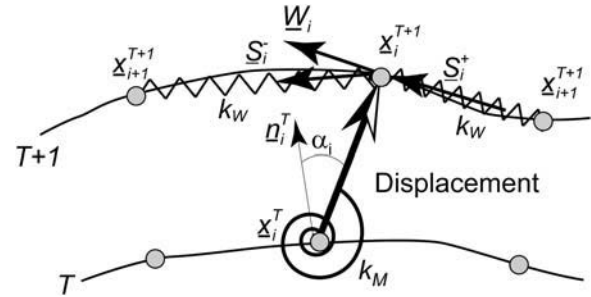

FIGURE 5   Measurement of boundary displacement vector $(\underline{x}_i^{\mathrm{T}} \rightarrow \underline{x}_i^{\mathrm{T+1}})$ by the mechanical method. The position of the marker $\underline{x}_i^{\mathrm{T+1}}$ is determined by the equilibrium of linear spring forces $\underline{S}_i^-, \underline{S}_i^+$ and a torsion spring force $\underline{W}_i$. The torsion spring enforces normal displacement in the direction $\underline{n}_i^{\mathrm{T}}$. The linear springs enforce regular spacing while maintaining the sequence order $(1,..,i-1,i,i + 1,...N)$ of markers (topological consistency).

defined two marker sets in the same sense of orientation and intrinsically determined their topology. Preservation of marker topology was enforced by prohibiting the exchange of positions of any particle pair $(\underline{x}_i^{\mathrm{T+1}} \underline{x}_{i+1}^{\mathrm{T+1}})$ in the directed sequence. The positions of the markers, and consequently the protrusion directions, were defined by the equilibrium of the spring system governed by

$$\underline{S}_i^- + \underline{S}_i^+ + \underline{W}_i = 0 \quad i = 1..N, \qquad (6)$$

where $\underline{S}_i^-$ and $\underline{S}_i^+$ were the linear spring forces between $\underline{x}_{i-1}^{\mathrm{T+1}}$ and $\underline{x}_i^{\mathrm{T+1}}$ and between $\underline{x}_i^{\mathrm{T+1}}$ and $\underline{x}_{i+1}^{\mathrm{T+1}}$, respectively, and $\underline{W}_i$ was the torsion spring force between $\underline{x}_i^{\mathrm{T}}$ and $\underline{x}_i^{\mathrm{T+1}}$. The direction of the unloaded torsion spring was chosen normal to the local boundary at T, and the length l of the unloaded linear springs was chosen to be $l = S/(N-1)$ where S was the boundary length between marker 1 and N. The forces are obtained by

$$\underline{S}_i^- = k_{\mathrm{s}} \left(\left\| \underline{x}_i^{\mathrm{T+1}} - \underline{x}_{i-1}^{\mathrm{T+1}} \right\| - l \right), \qquad (7)$$

$$\underline{S}_i^+ = k_{\mathrm{s}} \left(\left\| \underline{x}_{i+1}^{\mathrm{T+1}} - \underline{x}_i^{\mathrm{T+1}} \right\| - l \right), \qquad (8)$$

$$\underline{W}_i = k_{\mathrm{W}} / \pi \arccos(\alpha_i), \qquad (9)$$

where α_i is the angle between the normal to the boundary at $\underline{x}_i^{\mathrm{T}}$ and the displacement direction $(\underline{x}_i^{\mathrm{T}}, \underline{x}_i^{\mathrm{T+1}})$. Notice that for the calculation of the torsion spring force in Eq. 9 the distance between $\underline{x}_i^{\mathrm{T}}$ and $\underline{x}_i^{\mathrm{T+1}}$ is not accounted. Therefore, our mechanical system does not strictly follow physical laws. However, we found that this approach yielded the most stable results. By definition of Eq. 6 any marker i is coupled to the equations of the neighboring markers $i - 1$ and $i + 1$. The thus-constructed, nonlinear equation system was solved with a Marquard-Levenberg optimizing algorithm to estimate the unknown marker positions $\{\underline{x}_i^{\mathrm{T+1}}\}, i = 1 \ldots N$.

The only free parameters in this model were the linear spring constant k_{S} and the torsion spring constant k_{W}. To enforce topological consistency in the solution, the linear spring constant was designed with two regimes. The first regime is governed by the constant k_{S1} for marker pairs in the correct order and the second regime by the constant k_{S2} for marker pairs in reverse order. Extensive numerical experimentation indicated to us that enforcement of topological consistency is more delicate than marker propagation in the normal direction. In most situations, preservation of the correct order of markers implied marker propagations approximately normal to the cell boundary. Therefore, we chose $k_{\mathrm{S1}} = 1$, $k_{\mathrm{S2}} = 1000$, and $k_{\mathrm{W}} = 0.1$ to penalize topologically wrong solutions and to give the linear springs enforcing correct order more weight than the torsion springs. This set of parameter values guaranteed fast convergence to a stable solution with the least tendency to topological violations independent of the cell boundary shape.

Cell boundary detection

In this study all cell boundaries were extracted from fluorescence microscopy data. The boundary line was segmented applying global threshold level estimation separately to each frame. First, the image was filtered with a Gauss filter of width $\sigma = 1$ pixels. The threshold was then determined based on the intensity histogram of the filtered image. Typically, cell images obtained from fluorescence microscopy have a multimodal histogram distribution, where the first mode represents the background and the higher modes the cell. Therefore, for boundary segmentation it was sufficient to determine the local minimum between the first and second intensity modes. To achieve this robustly, nonrelevant extrema caused by local intensity variations had to be removed. We removed the lowest 0.5% of the low-intensity pixels and smoothed the histogram (supplemental Fig. 1 A, Supplementary Material). To avoid a phase shift in the histogram, which would change the position of the extrema, smoothing was performed bidirectionally. The Gauss filter width was dependent only on the bit depth of the image and was set to 3.8 intensity levels for 16-bit images. After thresholding, the image was filtered with a binary median filter of size 3×3 pixels and the boundary was treated with a disk-shaped closure operator of size 6 pixels (supplemental Fig. 1, B and C, Supplementary Material). After filling remaining holes inside the cell area and in the background the boundary was extracted from the segmented image.

Microscopy and sample preparation

All morphodynamic analyses in this article were performed on previously published cell images, which we selected due to their specific characteristics and molecular conditions and which were kindly provided to us by the authors of these articles.

Cells from all cell types where plated on glass substrates, except MEF/3T3 cells, which were plated on fibronectin-coated glass coverslips (10 μg/ml fibronectin for 1 h at 37°C; Sigma, St. Louis, MO). MEF and PtK1 cells were imaged in F-12 medium with 10% FBS, 25 mM HEPES, and antibiotics at 37°C. Primary cultures of newt lung epithelial cells were imaged in half-strength L-15 medium with 10% FCS and antibiotics at room temperature. Keratocytes were imaged in L-15 medium with 10% FBS and antibiotic/antimycotic at room temperature.

Further details on microscopy and sample preparation can be found in the original publications, as referenced in each figure caption: in Salmon et al. for newt lung epithelial cells (19), in Nalbant et al. for MEF (20), in Wittmann et al. (21) for PtK1 cells and Rac1 and PAK perturbations, and in Gupton et al. (22) for the Arp2/3 perturbations. Keratocytes were isolated from the scales of the central American cichlid *Hypsophrys nicaraguensis* as described by Kolega et al. (23), with the exception that the scales were sandwiched between two acid-washed glass 25-mm coverslips.

RESULTS AND DISCUSSION

Test problems

For protrusion and retraction tracking, large displacements and corrugated cell outlines with spikes such as filopodia or retraction fibers are the most difficult cases. To test the stability of the LSM under these conditions two benchmark tests were devised. The first was used to examine the LSM on boundaries with strong deformations and the second to examine the LSM on boundaries with spikes, which, due to their high curvature at the tip, can cause numerical instabilities. In both test cases the simpler mechanical method failed because of the strong shape deformation between frames. Therefore, we compared the two methods on less complex cell shapes (see next section).

The first test was an ellipse mapped onto a second ellipse rotated by 90°, so that one part of the ellipse was strongly protruding while the other part was retracting (Fig. 6). Three different speed functions were tested:

1. The cell boundary difference speed

$$F_{\mathrm{d}} = \phi_{\mathrm{t}} - \phi_{\mathrm{T}+1}. \qquad (10)$$

2. A sigmoidal function of the cell boundary difference, which dampens high speeds

$$F_{\mathrm{a}} = \mathrm{asinh}(\phi_{\mathrm{t}} - \phi_{\mathrm{T}+1}). \qquad (11)$$

3. A speed function controlled by the curvature κ of the cell boundary

$$F_{\kappa} = (\phi_{\mathrm{t}} - \phi_{\mathrm{T}+1})(\varepsilon + \kappa), \qquad (12)$$

where κ is calculated by a second-order central finite difference approximation to

$$\kappa = \frac{\phi_{xx}\phi_y^2 - 2\phi_y\phi_x\phi_{xy} + \phi_{yy}\phi_x^2}{(\phi_x^2 + \phi_y^2)^{3/2}}. \qquad (13)$$

According to Eq. 12, regions of the cell boundary with strong curvature evolve faster than regions with low curvature. This tends to straighten the boundary and prevents the formation of high curvature features in the evolution between flat boundary sections. The constant ε, which is set to $\varepsilon = 1/3$ for all our experiments, guarantees that concave boundary sectors do not move away from the target boundary (i.e., the sign of $(\phi_{\mathrm{t}} - \phi_{\mathrm{T}+1})$ is preserved for radii of curvature >3 pixels). The value of ε is determined by the computational grid size, which in our case was set to 3 pixels (see above). The smallest radius of curvature represented on a grid is the grid size itself. Therefore, this choice of ε imposes correct boundary motion for any cell shape that can be represented with the preset numerical resolution.

For all three speed functions, the cell boundary evolved until it accurately approximated the target shape. Although there was no significant difference in the protrusion rate obtained from the different speed functions, the boundary evolution and consequently the marker paths differed substantially (Fig. 6 A–G). The reason that the pathlength is insensitive to the path shape can be explained as follows. Assuming two straight paths, the difference in the pathlength can be approximated by $d \approx l(1/\cos(\alpha) - 1)$, where l is the pathlength and α is the difference in direction of the two paths. For small angles α the pathlength difference converges to zero since $\cos(\alpha) \approx 1$.

With F_{d} (Eq. 10), the protruding sector of the boundary underwent strong lateral dilation, while the retracting sector was compressed (Fig. 6 A). Apart from the question whether this amount of lateral membrane deformation is realistic in a cell, the marker distribution along the protruding section of the boundary diverged very unequally, lowering locally the spatial resolution of displacement measurements (Fig. 6 B).
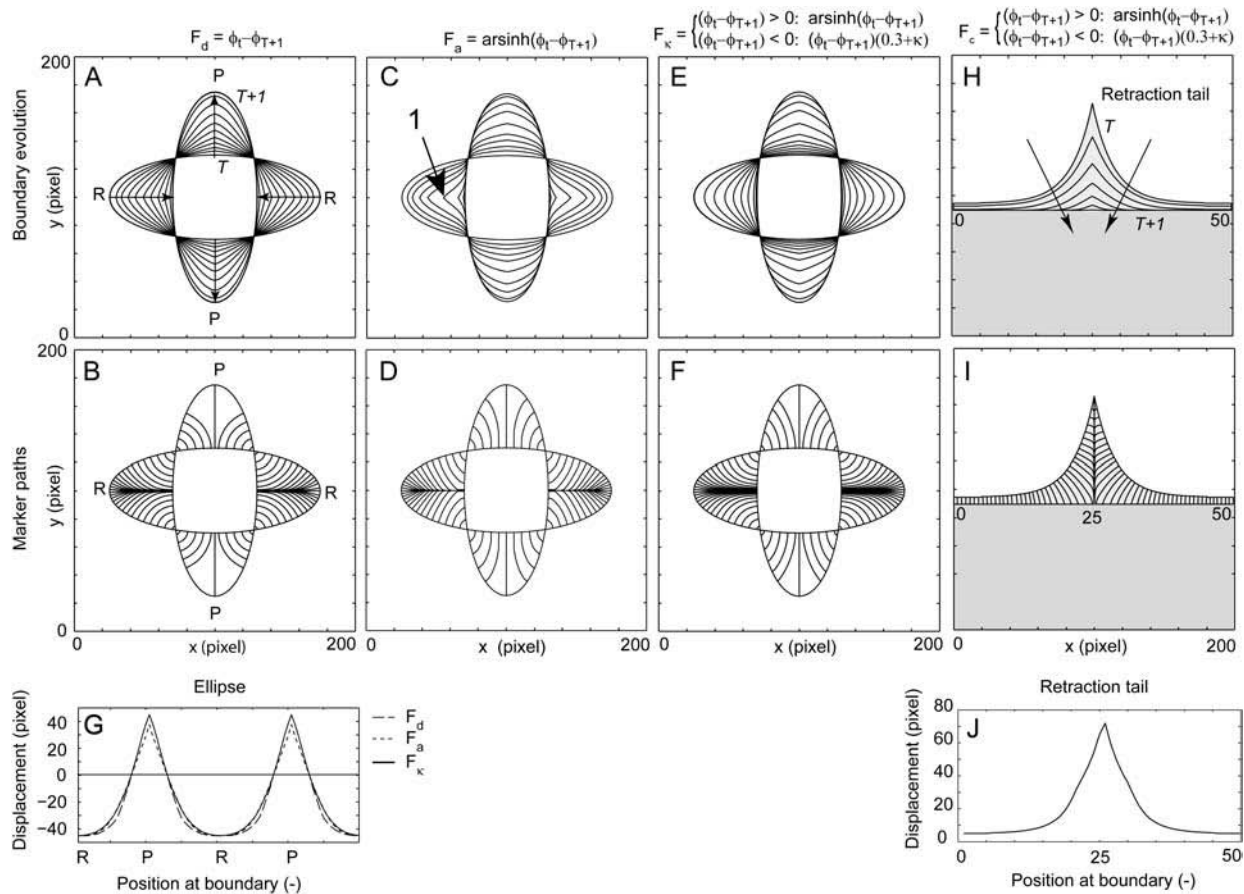
FIGURE 6　Evaluation of the LSM on two test cases using three different speed functions. The computational grid size was (3,3) pixels and the adaptable time step of the integrator was on average 0.1. See text for a discussion of the difference in speed functions.

By using the damped speed function F_a (Eq. 11), the propagation speed was more equal along the boundary, reducing the degree of lateral deformation (Fig. 6, C and D). However, the retracting part developed a corner during its evolution (Fig. 6 C, *arrow 1*). Therefore, to simultaneously obtain a moderate dilation in protruding regions and suppress the development of shape singularities in retracting regions, a combination of the damped speed function (Eq. 11) for protrusions and the curvature-controlled speed function (Eq. 12) for retractions was employed (Fig. 6, E and F). This combined speed function performed satisfactorily also on a simulated retraction fiber (Fig. 6, H–J).

Cell protrusion and retraction measurements

Next, we applied the LSM and the mechanical method to track boundary displacements of migrating mouse embryonic fibroblasts (MEFs). The magnification was $40\times$ and images were taken at 1-min intervals. In general, both methods yielded very similar marker paths (Fig. 7, A and B) and boundary displacement rates (Fig. 7 C). However, in regions of strong boundary deformation, the mechanical method failed to reconstruct a topologically consistent solution (Fig. 7 B,

arrowhead 1). In such cases the protrusion direction can significantly deviate from the normal direction, and, as a consequence, the linear springs are too weak compared to the torsion springs to enforce the correct order of markers along the boundary. Quite surprisingly, even in these regions the measured displacement did not substantially differ from the one obtained with the LSM (Fig. 7 C, *arrowhead 1*). This means that displacement measurements are robust against variations in the direction in which the measurement is taken even in cases where topological inconsistencies are introduced. However, it is evident that the mechanical method is more limited and eventually breaks down with strong boundary deformation. Critically, the point of breakdown is unknown a priori. In contrast, the LSM has no such inherent limitations. To illustrate this we measured the boundary displacement of the same cell but with a time interval of 10 min (Fig. 7, D and E). The close-up view (Fig. 7 F) shows that even in the areas of strong retraction a consistent solution without topological confusion was obtained.

In a second test the protrusion and retraction activity at the leading edge of a PtK1 epithelial cell was analyzed. The magnification was $100\times$ and images were taken at 10-s intervals. Even though the cell boundary was detected with
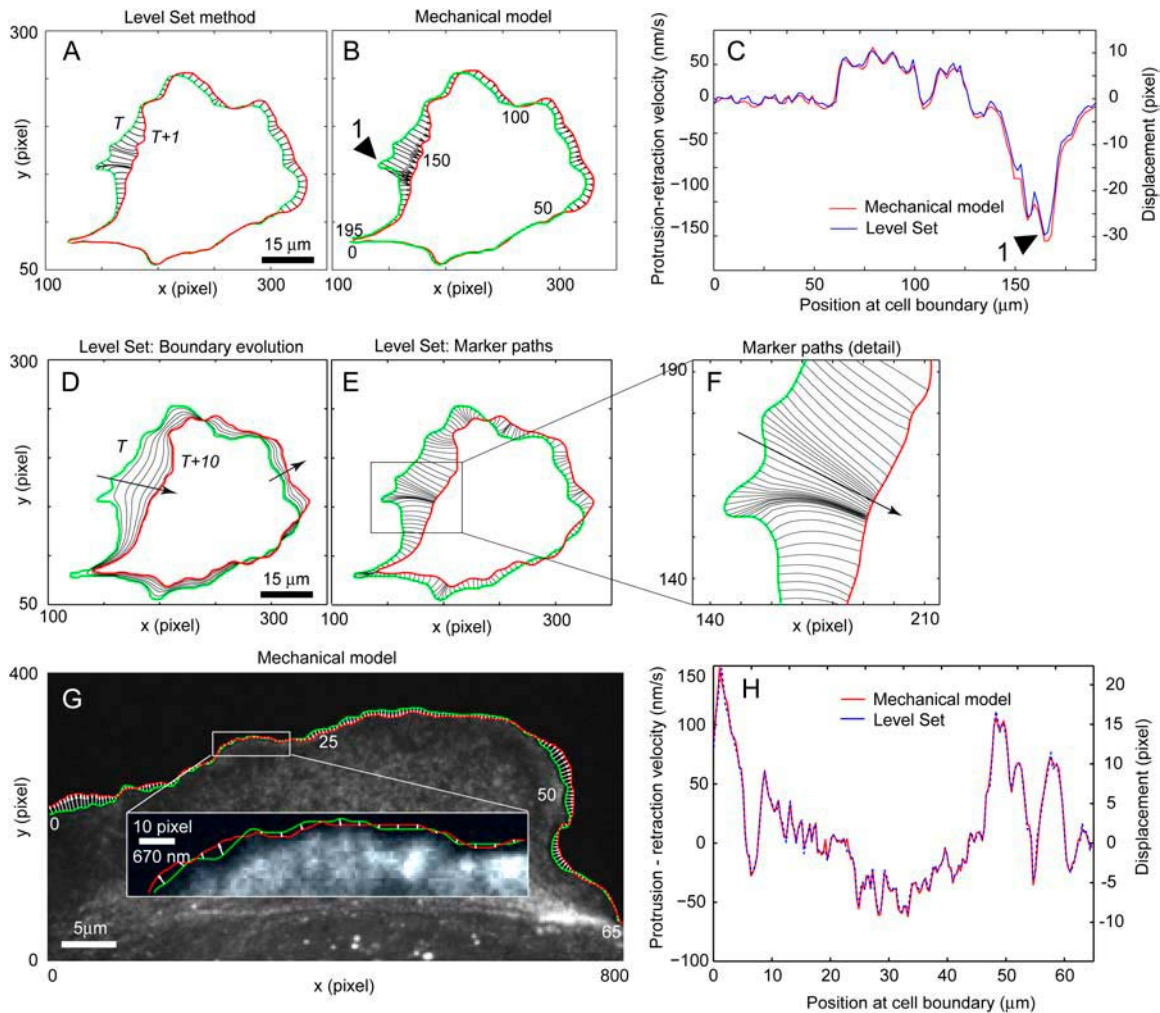
FIGURE 7 Evaluation of the LSM and the mechanical method on migrating cells. (*A–F*) Analysis of whole-cell movement of a MEF. Spatial resolution, 314 nm/pixel. Frame interval, 1 min. Image courtesy of O. Pertz. (*A*) Marker paths obtained from the LSM. (*B*) Displacement vectors obtained by the mechanical model. In the area of high boundary deformation (*arrowhead 1*), the method fails to deliver a topologically consistent solution. (*C*) Comparison of the two methods shows only small differences in the protrusion and retraction rates, despite the topological violation by the mechanical model. (*D*) Boundary evolution obtained by the LSM for the same cell but with a frame interval of 10 min. (*E*) Marker paths. (*F*) Detail showing the marker paths for a region of high boundary deformation. To accommodate the strong contraction of the cell membrane during retraction the marker paths became strongly curved and converged. (*G,H*) High-resolution analysis of the protruding boundary of a PtK1 cell. Spatial resolution, 67 nm/pixel. Frame interval, 10 s. (*G*) Displacement vectors obtained by the mechanical method. (*Inset*) Displacements of <1 pixel were resolved. (*H*) Comparison of protrusion and retraction rates obtained by LSM and mechanical method.

integer pixel accuracy, both methods resolved displacements <1 pixel ($\triangleq 67$ nm) (Fig. 7 *G, inset*). The resolution of displacement measurements is limited by two sources of error in the detection of the boundary position. The first term is related to image noise, which is approximately uncorrelated between pixels. Consequently, the spline filtering used to interpolate integer positions of segmented boundary pixels tend to represent the actual edge position with subpixel accuracy (24). The second error arises from the segmentation of the cell boundary through a global threshold level. Depending on the chosen level the detected boundary is shifted relative to the true edge position. However, because the threshold level distorts the boundary position equally for all images, the measurement of boundary displacements

between frames is not affected. We simulated displacements of synthetic binary objects and found that for shape undulations at a length scale similar to cell edge movements and noise levels comparable to the data used in this article spline interpolation provides sensitivity in detecting edge displacements in the range 0.1–0.2 pixels (data not shown). Evidence for this high sensitivity can also be found in morphodynamic activity maps of real experiments as introduced below (see Fig. 10 *C*). This activity map contains regions with boundary velocities of ± 5 nm/s, corresponding to displacements ± 0.7 pixels per frame. Because these regions describe consistent patterns that extend over several frames and over many independently measured locations along the cell boundary, these data cannot be due to random noise. Measurement noise

below the smallest resolvable displacement would lead to random positional variations of the cell boundary, clearly distinct from the high spatiotemporal organization of the patterns found in these activity maps.

To test the accuracy of the cell boundary evolution as approximated by the LSM we analyzed the boundary dynamics of a migrating MEF (Fig. 8 *A*). We calculated the evolution between time points $T = 1$ and $T = 10$ and compared the propagated boundary lines to the actual boundary positions at time points $T = 2, \ldots, 9$. We found that for boundary sections with a unidirectional motion the approximation was in good qualitative agreement with the actual boundary movement (Fig. 8, *B* and *C*, *arrowhead 1*). As expected, for regions where the boundary switched between protrusion and retraction the LSM failed to approximate the actual boundary movement (Fig. 8 *C*, *arrowhead 2*). This means that in cases where the frame rate is sufficient to resolve constant and unidirectional motion, the LSM gives a good approximation of the true boundary displacement. This is particularly the case in sections where a cell exhibits fast and generally unidirectional protrusion or retraction. These are precisely the sections where the application of the LSM is most required, because the time sampling might not be fast enough to capture trajectories of the high-speed movements. On the other hand, movements tend to directionally fluctuate in more quiescent sections of the cell boundary. Here, any simpler method could track the boundary equally well and the reconstruction of the movement becomes merely an issue of time sampling.
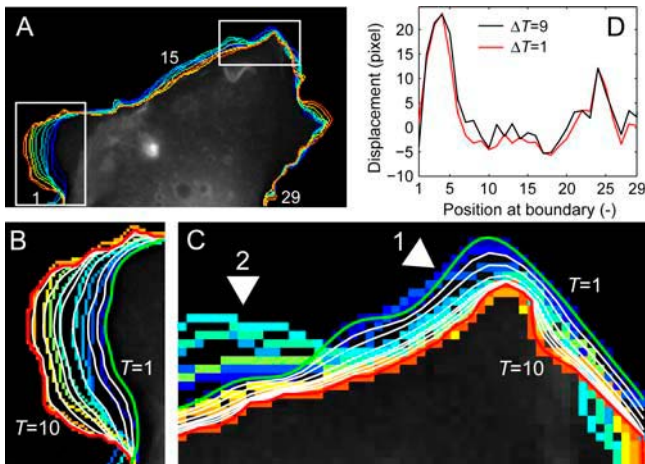
In case of an optimal reconstruction of the boundary evolution, displacement measurements would be independent of the chosen time step. In the example of Fig. 8, the displacement between $T = 1$ and N would thus be the same as the sum of displacements from $T = 1$ to 2, 3 to 4, $\ldots$, and $N - 1$ to N. We tested this on a series of 10 frames. We measured the displacement first as the sum of displacements using a frame interval of $\Delta T = 1$ and then directly with a frame interval of $\Delta T = 9$ (Fig. 8 *D*). For boundary sections with unidirectional motion both time steps delivered the same result up to maximal difference of ~1 pixels. In sections with switches in motion direction the difference was bigger (maximal 4 pixels), confirming our above assessment of the LSM.

Morphodynamics of different cell types

We compared the morphodynamics of migrating keratocytes and MEFs, as well as the local morphodynamics of protruding lamellipodia of newt lung epithelial (NLE) and PtK1 cells in a wound healing response. To visualize and classify cell morphodynamics we constructed activity maps in which protrusion and retraction rates are plotted in a ''time-cell boundary position'' coordinate system. Colors indicate the boundary speed at position s and time T (Fig. 9).

The activity map of keratocyte migration confirmed a persistent polarity between leading and trailing edges, but it also revealed that the tail retracted in an alternating fashion (Fig. 10 *A*, *circles*). Similarly, the MEF (movie 2) (Fig. 10 *B*) showed a strong polarization and was able to maintain the sharp division between actively protruding and quiescent regions of the cell boundary over 16 min. This suggests that the molecular factors that establish cell polarity can remain spatially confined over an extended period, a finding that

FIGURE 8 Evaluation of the LSM edge interpolation. (*A*) Segmented boundaries from 10 time points of a migrating MEF. Cell outlines are time color coded. (*blue*) Early time points; (*red*) late time points. Frame interval, 20 s. (*B*) Detail of a boundary section with unidirectional motion. The boundary evolution from $T = 1$ to $T = 10$ obtained from the LSM (*white lines*) overlaid on the segmented boundaries at $T=1,2\ldots9,10$. (*C*) Detail of a boundary section with switching between protrusions and retractions. (*D*) Displacements of the cell boundary from $T = 1$ until $T = 10$, measured once using a frame interval of $\Delta T = 1$ (*black curve*) and once using a frame interval of $\Delta T = 9$ (*red curve*). Image courtesy of O. Pertz.
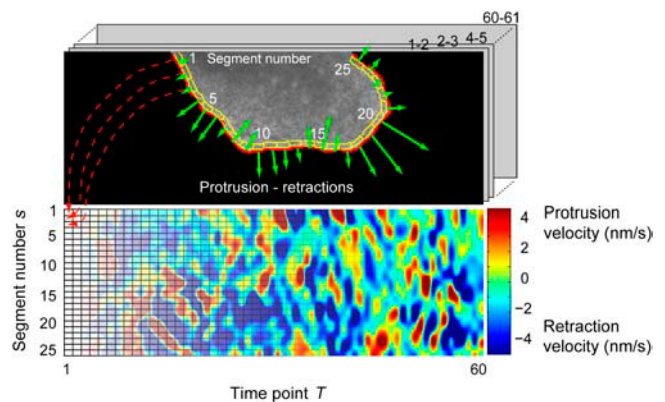

FIGURE 9 Construction of morphodynamic activity maps. Boundary displacements between frames 1 and 2 were filled into the first column of the activity map. The same procedure was repeated for the following time steps. The color at (s,T) encodes the displacement velocity at time point T and boundary segment s. To reduce the noise, activity maps were filtered in the time direction using smoothing splines with a smoothing factor corresponding to a Gaussian filter width of ~2 time steps.
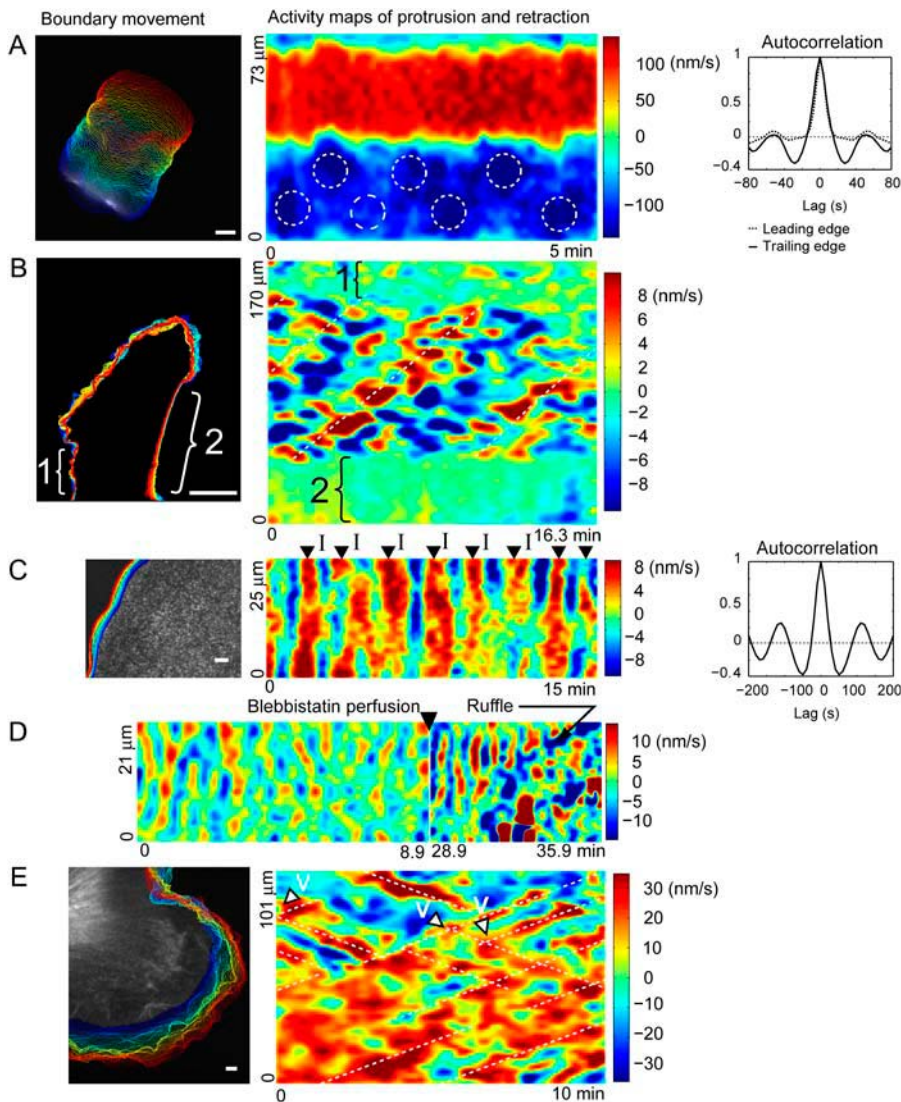
FIGURE 10 Comparison of morphodynamic patterns in different cell types. (*A*) Activity map of a migrating keratocyte indicating a persistent polarity of the leading and trailing edge. Cell protrusion at the leading is uniform, whereas retraction at the trailing edge occurs with a left-right periodicity (*circles*). Scale bar = 10 μm. Autocorrelation of the morphodynamics of leading edge and trailing edge. Image courtesy of P. Yam, C. Wilson, and J. Theriot. (*B*) MEFs exhibited a distinct and persistent separation of active (*bracket 1*) and quiescent (*bracket 2*) boundary regions. Activity maps revealed transversal protrusion waves traveling with constant speed along the cell boundary (*dashed lines*). Scale bar = 20 μm. Image courtesy of O. Pertz. (*C*) Leading edge protrusion of a NLE cell. The boundary was oscillating in a coordinated fashion (*I-state*) with a remarkably constant frequency of 100 s (cf. autocorrelation). Scale bar = 3 μm. (*D*) Leading edge protrusion of a NLE cell before and after perfusion with blebbistatin. Waiting time after perfusion before morphological profiling was 20 min. The drug treatment had no effect on the morphodynamic state of the NLE cell and did not markedly change the periodicity of the *I-state*. Image courtesy of C. Waterman-Storer. (*E*) Leading edge protrusion of a PtK1 epithelial cell. Morphodynamic patterns resulted from a superposition of transversal protrusion waves traveling with constant speed along the boundary (*V-state*). Scale bar = 3 μm. Image courtesy of J. Lim.

agrees with current models that propose membrane compartmentalization (25). In contrast to the keratocyte, the MEF leading edge morphology was more dynamic. We found that periodic waves (period $T = 8$ min) of protrusion and retraction traveled along the cell boundary with a constant speed of 10.2 μm/min (Fig. 10 *B*, *dashed lines*).

Next, we mapped the leading edge morphodynamics of NLE cells (movie 3). Again we observed waves of protrusion and retraction (period $T = 1.8$ min). Unlike in MEFs, the waves were synchronized along the edge, resulting in an activity pattern we referred to as the *I-state* (*arrowheads I*, Fig. 10 *C*). In contrast, Ptk1 epithelial cells displayed a seemingly chaotic and uncoordinated protrusion activity (movie 4). However, the activity map (Fig. 10 *E*) indicated that this complex pattern originated from a superposition of protrusion waves traveling in opposite directions laterally along the cell boundary with a speed of 5.9 μm/min. The protrusion waves initiated from different points of the

boundary from which they propagated in both directions (Fig. 10 *E*, *arrowheads*). Accordingly, we refer to this morphodynamic pattern as the *V-state*.

The characteristics of propagating waves had a surprisingly low variability over time as well as among cells, despite the differences in trajectories and the seemingly random, exploratory protrusion behavior (Fig. 11, movies 5–8). The propagation speed of the transversal waves was 8.2 $\pm$ 3 μm/min ($n = 5$) and independent of the migration velocity of cells. This suggested the existence of a universal, organizational principle behind the protrusion patterns of migrating cells.

Perturbations of Rac1 and its effectors alter the protrusion state

What is the molecular mechanism that leads to either synchronous (*I-state*) or transversally propagating (*V-state*)
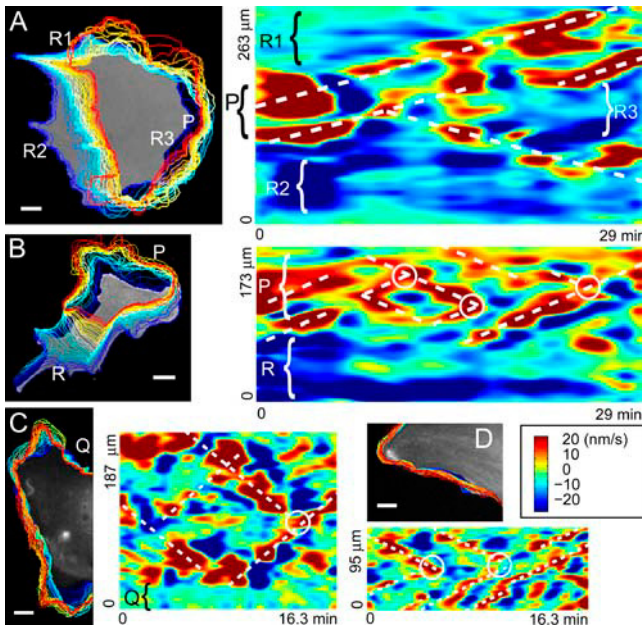
FIGURE 11 Comparison of protrusion and retraction activity maps from MEFs to demonstrate low variability in morphodynamic patterns despite significantly different cell outline shapes. (*A,B*) Activity maps of entire cells. Leading edge of the cell is indicated with *P* and trailing edge with *R*. Transversal wave propagation speeds are 4.2 and 6.3 μm/min (movies 5 and 6). (*C,D*) Activity maps of the leading edge of polarized, but slowly migrating MEFs. Note that the leading edge activity is the same as for the migrating cells. Transversal wave propagation speeds 12 and 8.2 μm/min (movies 7 and 8). Quiescent region is indicated with *Q*. Scale bars = 10 μm.

waves of protrusion and retraction? *I-state* waves have also been documented in MEF cell spreading assays (26,27). The wave period observed in these studies was 24 ± 7 s and 17 ± 4 s, respectively, in contrast to our measurement of 100 s in NLE cells. In both these articles wave formation was explained via self-perpetuated, periodic actomyosin network contractions. To test the possibility whether the generation of *I-state* waves in migrating NLE cells obeys the same molecular mechanisms as in spreading MEF, we treated NLE cells with blebbistatin, a direct inhibitor of the ATPase activity of myosin II (28). As illustrated in Fig. 10 *D*, blocking myosin activity had no effect on the morphodynamic state of the NLE cell, nor did it markedly change the periodicity of the *I-state*. Thus, we have concluded that the *I-state* observed in the protrusion of migrating NLE cells is mechanistically different from the periodic spreading of MEFs.

Protrusion is thought to be driven by the assembly of a dendritic network of actin filaments (14). Transversal protrusion waves similar to our *V-state* have in fact been observed in *Dyctostelium* motility (29) and were later brought into connection with reaction-diffusion waves of actin polymerization and depolymerization (30). In a very recent study, we have described the periodicity of lamellipodium actin network assembly in NLE cells, which were identical to the periodicity of the *I-state* (31). Hence, we speculated that

the observed protrusion pattern could be mediated by actin polymerization waves and that the morphodynamic differences between the *I-* and the *V-states* could be associated by differences in the activation of actin assembly.

In view of the well-established regulation of lamellipodial actin polymerization by Rac1 via stimulation of Arp2/3 (32–38), we hypothesized that the differences between *I-* and *V-state* could depend on the level of Rac1 activity. To test this we measured the morphodynamics of control PtK1 cells (Fig. 12 *A*) and PtK1 cells expressing constitutively active Rac1(Q61L) (Fig. 12 *B*). Indeed, this intervention switched the *V-state* in control cells into the *I-state*. From these data, we conclude that in control cells Rac1 activation defines the rate-limiting step in the transversal propagation of protrusion waves. In the presence of Rac1(Q61L) spontaneous initiation of protrusion in one place of the leading edge causes a quasi-instantaneous propagation of the protrusion wave, so that the edge activity appears synchronized over long sections of the boundary at the spatial and temporal resolution available in our movies.

Constitutively active Rac1 did not lead to permanent protrusion activity, but the alternation of protrusion and retraction phases was preserved. Also the duration of the phases in *V-* and *I-states* was similar. This suggests a mechanism that antagonizes Rac1-activated actin polymerization and is directly coupled to Rac1, i.e., elevated Rac1 activation does not only raise the amount of stimulated Arp2/3 but at the same time limits the rate of polymerization so that the net amount of network assembly in one protrusion-retraction cycle remains constant and independent of the absolute level of active Rac1. One candidate molecule for such an autoinhibitory protrusion mechanism is the Rac1-effector PAK. Increased PAK activity blocks polymerization via activation of LIM-kinase, which, in turn, inactivates cofilin (36), leading to depletion of polymerizable G-actin. To test this model we inhibited PAK through its PID(H83L) domain (Fig. 12 *C*). In the absence of functional PAK the entire leading edge protruded persistently at a significantly higher rate (~30 nm/s) compared to control cells and cells expressing constitutively active Rac1 (~15 nm/s). Other than in control cells, boundary retraction occurred through ruffles traveling laterally along the cell boundary, creating a new morphodynamic pattern. In contrast to protrusion waves, which start at one point and typically travel in both directions, retraction waves traveled only in one direction. The propagation of retraction waves continued until they collided with a second retraction wave traveling in the opposite direction, forming an upside down "V" pattern. Thus, we refer to this morphodynamics as the *λ-state*. It is not clear by which events ruffles are initiated and by which mechanisms they propagate along the leading edge.

In a model where Rac1 activates actin assembly, but at the same time also initiates an autoinhibitory mechanism, one would expect that the persistence of transversally propagated protrusion waves depends on the availability of resources for
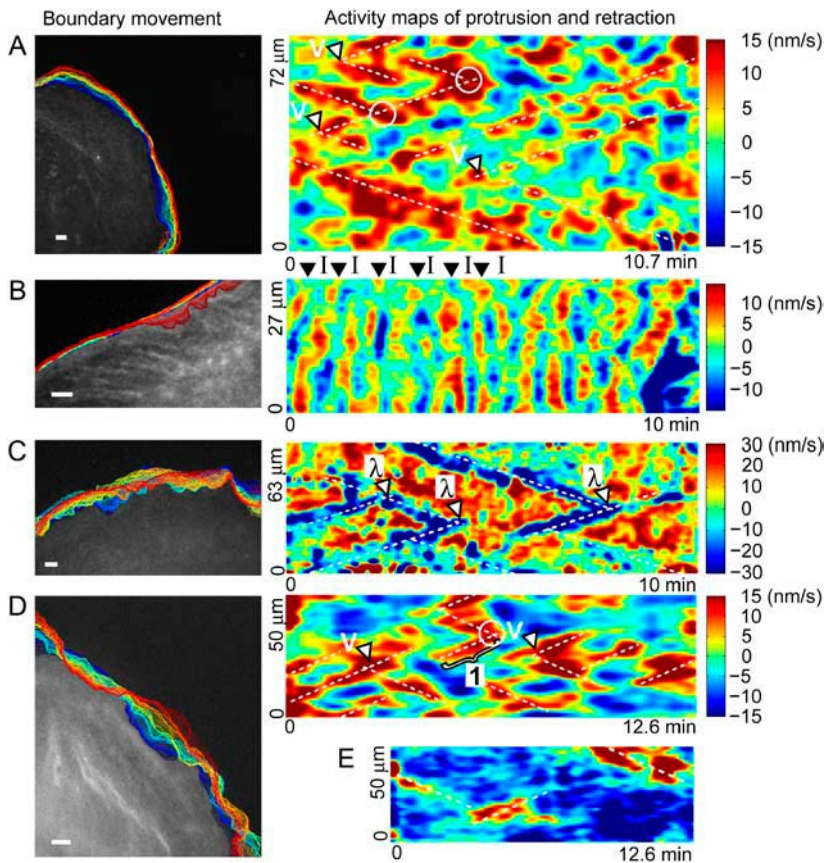
FIGURE 12 Perturbation analysis of morphodynamic patterns in PtK1 epithelial cells. (*A*) Control cell characterized by *V-state*. Image courtesy of J. Lim. (*B*) PtK1 cell expressing constitutively active Rac1(Q61L). It phenocopies the *I-state* of NLE cells (cf. Fig. 10 *C*). Image courtesy of T. Wittmann. (*C*) PtK1 cell expressing Rac1(Q61L) and with PAK inhibition. The cell turns into a hyperactivated protrusion state mediated by permanent actin polymerization. This protrusion state is only interrupted by transversally propagating ruffles leading to short-term retraction of the edge. Image courtesy of V. Delorme. (*D,E*) PtK1 cell with inhibited Arp2/3. This intervention maintains the *V-state* but fewer and less persistent waves are initialized. Bracket 1 indicated typical wave persistence duration of 2 min. The propagation speed of these waves was not affected by Arp2/3 inhibition. Image courtesy of S. Gupton. Scale bar = 3 μm.

actin polymerization downstream of Rac1. Qualitatively, this is supported in control cells by the observation that protrusion waves traveling toward each other do rarely intersect but disappear after collision (Figs. 12 *A*, *circles*, and 11, *B–D*, *circles*). One explanation for this are the depleted polymerization resources in the wake of a protrusion wave, preventing continuing propagation of two meeting wave fronts traveling in opposite directions. Before a new protrusion wave can pass the region of a previously protruding section of the cell boundary, polymerization resources have to be replenished by diffusion or active transport (5). How fast the replenishment occurs can be inferred from the time lag between two successive waves at a certain location (70–100 s). Quite interestingly, the time lags are similar for the *I*- and the *V-state*, supporting the idea that periodicity and persistence but not the speed of the waves are dependent on the local concentration of polymerization resources (e.g., Arp2/3, and/or polymerizable G-actin).

To test this model directly and more quantitatively, we inhibited activation of Arp2/3 downstream of Rac1 by overexpression of the CA domain of N-Wasp. The morphodynamic activity maps of these cells (Fig. 12, *D* and *E*) still exhibit spurious protrusions, but they occur less frequently and their propagation along the cell edge is clearly less persistent (2 min as compared to >6 min in control cells; Fig. 12 *D*, *bracket 1*). However, the propagation speed of the

wave remained unchanged. This suggests that a critical level of Arp2/3 is required to maintain the propagation of protrusion waves but that the propagation velocity is essentially determined by the level of Rac1 activation.

To summarize, our morphodynamic profiling method reveals the self-propagation of protrusion waves along the leading edge of epithelial cells. Perturbation analyses varying the levels of active Rac1 and Arp2/3 directly and G-actin concentration indirectly via PAK inhibition strongly suggest a dependence of protrusion wave formation on localized modulation of actin polymerization (Fig. 13). The precise mechanism of self-propagation remains elusive from our data and shall be the subject of future perturbation studies. However, given that stimulation of integrin signals is an established factor of Rac1 activation (39–42) we purport a working model where force feedback induced by actin assembly at the plasma membrane closes the loop necessary for wave propagation. Forces counteracting Rac-mediated elongation of actin filaments against the plasma membrane may lead to mechanical activation of integrins in nascent adhesion complexes, which in turn reinforce Rac1 activation. Locally, the positive feedback is broken by limited resources for polymerization (activated Arp2/3 and polymerizable G-actin) providing an explanation for the temporal propagation of alternating phases of protrusion and retraction. Transversal propagation of a protrusion wave could be
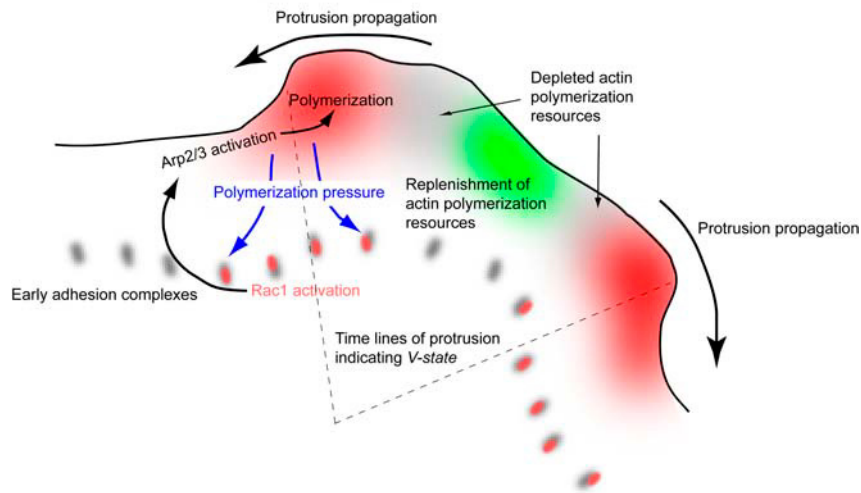
FIGURE 13 Mechanism of Rac1 dependent propagation of protrusion waves. A random burst of polymerization initiates protrusion waves propagating transversally in both directions. The waves are self-sustained by a feedback mechanism where polymerization pressure activates Rac1 at adhesion sites, which triggers Arp2/3 mediated polymerization. Polymerization pressure exerts a force onto the actin network. Due to network viscoelastic properties, the load is distributed onto adhesion complexes not only right behind the protrusion region but also in a lateral vicinity, leading to lateral propagation of the feedback mechanism. Locally polymerization lasts until resources are depleted. After critical resources for polymerization are renewed in the depleted region a new wave can be initiated. This protrusion propagation mode leads to the *V-state* as observed in the experiments (cf. Fig. 10 *D*).

explained by transmission of polymerization forces through the actin network in all directions, so that laterally neighboring adhesion sites are mechanically coactivated. Given the dominantly elastic characteristics of the actin network (43) and the short distance between the leading edge and the site of nascent adhesion formation, force transmission is likely to be fast, so that the activation of Rac1 in response to mechanical stimulation of adhesion complexes defines the rate-limiting step for protrusion wave propagation, as observed with the switch from the *V-state* to the *I-state* when expressing constitutively active Rac1. To conclusively test this model it will be necessary to probe transients in Rac1 at the same spatiotemporal resolution as the morphodynamic measurements and to simultaneously intervene with pathways that link mechanical stimulation of adhesion complexes to Rac1 activation, as achieved in very recent work by Pankov et al. (44). These authors identified Rac1 as a tunable switch between different motile and protrusive dynamics, very similar to our observations. They found that cells expressing constitutively active Rac1 develop a smooth and slow protruding cell edge. For isolated cells this can lead to loss of cell polarity and complete inhibition of migration. This state is equivalent to the *I-morphodynamic state* we describe in this article. At intermediate Rac1 levels, they observed random protrusions causing the cell to migrate in a jerky fashion at medium velocity. We suspect that this state is identical to the *V-morphodynamic state*, although the absence of a morphodynamic classification in Pankov et al. (44) does not permit a comparison of the spatiotemporal organization of these protrusion states.

CONCLUSIONS

We developed a framework for the measurement of cell morphodynamics with high spatial resolution. Patterns in spatiotemporal protrusion activity maps revealed a high level of organization with self-propagating waves of protrusion and retraction. Wave parameters such as initiation frequency, periodicity, and propagation velocity exhibited remarkably low variability among cells and allowed us to distinguish two main morphodynamic phenotypes. Perturbation of molecular pathways involved in actin polymerization had a direct impact on the morphodynamics allowing us to derive an initial working model of the mechanism of protrusion wave propagation. Our data support a model where the activation level of Rac1 controls the propagation velocity. The lateral persistence of protrusion waves depends on the relative abundance of activated Arp2/3 and polymerizable G-actin.

Methodologically, these morphodynamic data rely on a definition of protrusion and retraction as the boundary displacement between two time points, integrated continuously along the direction normal to the moving cell edge. Following this definition, we developed the LSM, which guaranteed topologically correct protrusion measurements over an unlimited dynamic range by estimating the intermediate states of the cell outline based on an evolutionary equation. More important, our definition of protrusion and retraction as well as the LSM is readily applicable to the measurement of boundary displacements in three dimensions, where the distinction of morphodynamic phenotypes in cell migration will be even more difficult than in two dimensions and where visual inspection breaks down. We analyzed data with boundary displacements in the range between 0.5 and 30 pixels per time step on cells with a diameter between 150 and 1000 pixels. Besides the absence of any limitation in terms of cell shape and deformation, the LSM bears the additional strength of being parameter-free. No adjustments have to be made for measurements on cells of different size, shape, or range of displacement. Another strength of the LSM is that different models of boundary evolution can easily be adapted by adjusting the speed function in Eq. 1. The physics of plasma membrane and cortex deformation is very complex and still little understood

on a quantitative level. Yet, we found that the simplistic assumption of a plasma membrane moving essentially proportional to the product of distance to the boundary at the next time point and local membrane curvature is sufficient to reconstruct a realistic boundary evolution between two time points. Even though with the LSM a stable solution is obtained for any time step in the image series it is important that the time step is chosen according to the specific morphodynamic phenomena that are studied. With significant undersampling critical events can be missed that cannot be recovered by methods relying only on edge tracking.

The implementation of a stable numerical algorithm of the evolution equation can make the LSM difficult to realize. For this reason we developed the mechanical method that provided, for moderate boundary deformations, excellent approximations to our definition of protrusion and retraction without topological violations.

SUPPLEMENTARY MATERIAL

An online supplement to this article can be found by visiting BJ Online at http://www.biophysj.org.

REFERENCES

1. Wessels, D., and D. R. Soll. 1998. Computer-assisted characterization of the behavioral defects of cytoskeletal mutants of Dictyostelium discoideum. *In* Motion Analysis of Living Cells. Wiley-Liss, Hoboken, NJ. 101–140.

2. Heid, P. J., J. Geiger, D. Wessels, E. Voss, and D. R. Soll. 2005. Computer-assisted analysis of filopod formation and the role of myosin II heavy chain phosphorylation in Dictyostelium. *J. Cell Sci.* 118:2225–2237.

3. Waterman-Storer, C. M., R. A. Worthylake, B. P. Liu, K. Burridge, and E. D. Salmon. 1999. Microtubule growth activates Rac1 to promote lamellipodial protrusion in fibroblasts. *Nat. Cell Biol.* 1:45–50.

4. Dunn, G. A., and D. Zicha. 1995. Dynamics of fibroblast spreading. *J. Cell Sci.* 108:1239–1249.

5. Zicha, D., I. M. Dobbie, M. R. Holt, J. Monypenny, D. Y. H. Soong, C. Gray, and G. A. Dunn. 2003. Rapid actin transport during cell protrusion. *Science.* 300:142–145.

6. Biyasheva, A., T. Svitkina, P. Kunda, B. Baum, and G. Borisy. 2003. Cascade pathway of filopodia formation downstream of SCAR. *J. Cell Sci.* 117:837–848.

7. Ghosh, M., X. Song, G. Mouneimne, M. Sidani, D. S. Lawrence, and J. S. Condeelis. 2004. Cofilin promotes actin polymerization and defines the direction of cell motility. *Science.* 304:743–746.

8. Rottner, K., B. Behrendt, J. V. Small, and J. Wehland. 1999. VASP dynamics during lamellipodia protrusion. *Nat. Cell Biol.* 1:321–322.

9. Rotsch, C., K. Jacobson, and M. Radmacher. 1999. Dimensional and mechanical dynamics of active and stable edges in motile fibroblasts investigated by using atomic force microscopy. *Proc. Natl. Acad. Sci. USA.* 96:921–926.

10. Totsukawa, G., Y. Wu, Y. Sasaki, D. J. Hartshorne, Y. Yamakita, S. Yamashiro, and F. Matsumura. 2004. Distinct roles of MLCK and ROCK in the regulation of membrane protrusions and focal adhesion dynamics during cell migration of fibroblasts. *J. Cell Biol.* 164:427–439.

11. Bear, J. E., T. Svitkina, M. Krause, D. A. Schafer, J. J. Loureiro, G. A. Strasser, I. V. Maly, O. Y. Chaga, J. A. Cooper, G. G. Borisy, and F. B. Gertler. 2002. Antagonism between Ena/VASP proteins and actin filament capping regulates fibroblast motility. *Cell.* 109:509–521.

12. Hinz, B., W. Alt, C. Johnen, V. Herzog, and H.-W. Kaiser. 1999. Quantifying lamella dynamics of cultured cells by SACED, a new computer-assisted motion analysis. *Exp. Cell Res.* 251:234–243.

13. Dubin-Thaler, B. J., G. Giannone, H.-G. Dobereiner, and M. P. Sheetz. 2004. Nanometer analysis of cell spreading on matrix-coated surfaces reveals two distinct cell states and STEPs. *Biophys. J.* 86:1794–1806.

14. Pollard, T. D., and G. G. Borisy. 2003. Cellular motility driven by assembly and disassembly of actin filaments. *Cell.* 112:453–465.

15. Osher, S., and J. A. Sethian. 1988. Fronts propagating with curvature-dependent speed: algorithms based on Hamilton-Jacobi formulations. *J. Comput. Phys.* 79:12–49.

16. Crandall, M. G., and P. L. Lions. 1984. Two approximations of solutions of Hamilton-Jacobi equations. *Math. Comput.* 43:1–19.

17. Osher, S., and C.-W. Shu. 1991. High order essentially non-oscillatory schemes for Hamilton-Jacobi equations. *SIAM J. Numer. Anal.* 28:902–921.

18. Harten, A., B. Engquist, S. Osher, and S. Chakravarthy. 1987. Uniformly high-order accurate essentially non-oscillatory schemes III. *J. Comp. Phys.* 71:231–303.

19. Salmon, W. C., M. C. Adams, and C. M. Waterman-Storer. 2002. Dual-wavelength fluorescent speckle microscopy reveals coupling of microtubule and actin movements in migrating cells. *J. Cell Biol.* 158:31–37.

20. Nalbant, P., L. Hodgson, V. Kraynov, A. Toutchkine, and K. M. Hahn. 2004. Activation of endogenous Cdc42 visualized in living cells. *Science.* 305:1615–1619.

21. Wittmann, T., G. M. Bokoch, and C. M. Waterman-Storer. 2003. Regulation of leading edge microtubule and actin dynamics downstream of Rac1. *J. Cell Biol.* 161:845–851.

22. Gupton, S. L., K. L. Anderson, T. P. Kole, R. S. Fischer, A. Ponti, S. E. Hitchcock-DeGregori, G. Danuser, V. M. Fowler, D. Wirtz, D. Hanein, and C. M. Waterman-Storer. 2005. Cell migration without a lamellipodium: translation of actin dynamics into cell movement mediated by tropomyosin. *J. Cell Biol.* 168:619–631.

23. Kolega, J. 1986. Effects of mechanical tension on protrusive activity and microfilament and intermediate filament organization in an epidermal epithelium moving in culture. *J. Cell Biol.* 102:1400–1411.

24. Duda, R. O., P. E. Hart, and D. G. Stork. 2001. Pattern Classification. John Wiley & Sons, New York.

25. Simons, K., and D. Toomre. 2000. Lipid rafts and signal transduction. *Nat. Rev. Mol. Cell Biol.* 1:31–39.

26. Giannone, G., B. J. Dubin-Thaler, H.-G. Dobereiner, N. Kieffer, A. R. Bresnick, and M. P. Sheetz. 2004. Periodic lamellipodial contractions correlate with rearward actin waves. *Cell.* 116:431–443.

27. Dobereiner, H.-G., B. J. Dubin-Thaler, G. Giannone, H. S. Xenias, and M. P. Sheetz. 2004. Dynamic phase transitions in cell spreading. *Phys. Rev. Lett.* 93:108105.

28. Straight, A. F., A. Cheung, J. Limouze, I. Chen, N. J. Westwood, J. R. Sellers, and T. J. Mitchison. 2003. Dissecting temporal and spatial control of cytokinesis with a myosin II inhibitor. *Science.* 299:1743–1747.

29. Killich, T., P. Plath, X. Wei, H. Bultmann, L. Rensing, and M. Vicker. 1993. The locomotion, shape and pseudopodial dynamics of unstimulated Dictyostelium cells are not random. *J. Cell Sci.* 106: 1005–1013.

30. Vicker, M. G. 2000. Reaction-diffusion waves of actin filament polymerization/depolymerization in Dictyostelium pseudopodium extension and cell locomotion. *Biophys. Chem.* 84:87–98.

31. Ponti, A., A. Matov, M. Adams, S. Gupton, C. M. Waterman-Storer, and G. Danuser. 2005. Periodic patterns of actin turnover in lamellipodia and lamellae of migrating epithelial cells analyzed by quantitative fluorescent speckle microscopy. *Biophys. J.* 89:3456–3469.

32. Steffen, A., K. Rottner, J. Ehinger, M. Innocenti, G. Scita, J. Wehland, and T. Stradal. 2004. Sra-1 and Nap1 link Rac to actin assembly driving lamellipodia formation. *EMBO J.* 23:749–759.

33. Hall, A. 1998. Rho GTPases and the actin cytoskeleton. *Science.* 279:509–514.

34. Ridley, A. J. 2001. Rho family proteins: coordinating cell responses. *Trends Cell Biol.* 11:471–477.

35. Miki, H., H. Yamaguchi, S. Suetsugu, and T. Takenawa. 2000. IRSp53 is an essential intermediate between Rac and WAVE in the regulation of membrane ruffling. *Nature.* 408:732–735.

36. Bokoch, G. M. 2003. Biology of the P21-activated kinases. *Annu. Rev. Biochem.* 72:743–781.

37. Machesky, L. M., and R. H. Insall. 1998. Scar1 and the related Wiskott-Aldrich syndrome protein, WASP, regulate the actin cytoskeleton through the Arp2/3 complex. *Curr. Biol.* 8:1347–1356.

38. Miki, H., S. Suetsugu, and T. Takenawa. 1998. WAVE, a novel WASP-family protein involved in actin reorganization induced by Rac. *EMBO J.* 17:6932–6941.

39. Price, L. S., J. Leng, M. A. Schwartz, and G. M. Bokoch. 1998. Activation of Rac and Cdc42 by integrins mediates cell spreading. *Mol. Biol. Cell.* 9:1863–1871.

40. Schwartz, M. A., and S. J. Shattil. 2000. Signaling networks linking integrins and Rho family GTPases. *Trends Biochem. Sci.* 25:388–391.

41. Bershadsky, A. D., N. Q. Balaban, and B. Geiger. 2003. Adhesion-dependent cell mechanosensitivity. *Annu. Rev. Cell Dev. Biol.* 19:677–695.

42. Tzima, E., M. A. Del Pozo, W. B. Kiosses, S. A. Mohamed, S. Li, S. Chien, and M. A. Schwartz. 2002. Activation of Rac1 by shear stress in endothelial cells mediates both cytoskeletal reorganization and effects on gene expression. *EMBO J.* 21:6791–6800.

43. Janmey, P. A., and D. A. Weitz. 2004. Dealing with mechanics: mechanisms of force transduction in cells. *Trends Biochem. Sci.* 29:364–370.

44. Pankov, R., Y. Endo, S. Even-Ram, M. Araki, K. Clark, E. Cukierman, K. Matsumoto, and K. M. Yamada. 2005. A Rac switch regulates random versus directionally persistent cell migration. *J. Cell Biol.* 170:793–802.